

Determination of fringe order in white-light interference microscopy

Peter de Groot, Xavier Colonna de Lega, Jim Kramer, and Michael Turzhitsky

Combining phase and coherence information for improved precision in white-light interference microscopy requires a robust strategy for dealing with the inconsistencies between these two types of information. We correct for these inconsistencies on every measurement by direct analysis of the difference map between the coherence and the phase profiles. The algorithm adapts to surface texture and noise level and dynamically compensates for optical aberrations, distortions, diffraction, and dispersion that would otherwise lead to incorrect fringe order. The same analysis also provides the absolute height data that are essential to relational measurements between disconnected surfaces. © 2002 Optical Society of America

OCIS codes: 120.3180, 120.3940, 150.3040, 120.6650, 150.6910.

1. Introduction

A small revolution in interference microscopy took place one decade ago, when conventional phase-shifting interferometry (PSI) that uses narrow spectral filters or lasers gave way to more-powerful and -flexible scanning white-light interferometry (SWLI). SWLI, also known as vertical scanning or coherence radar, takes advantage of the fringe localization in low-coherence interferometers to profile surfaces even when phase data have uncertain fringe order. The transition to white light has been facilitated by advances in precision mechanics and in camera and computer technology, which make it possible to rapidly acquire and analyze complicated interference patterns across thousands of image pixels.

The initial impetus to develop white-light microscopy as a computerized, quantitative tool was the similarity between coherence-based profiling and confocal microscopy.^{1,2} The subsequent realization that an optically rough surface is also accessible to white-light interferometry³ led to the extension of the technique to industrial surfaces, including ground metallic parts, ceramics, plastics, and even paper.⁴ From this development stage it was not long before it

was thought to integrate coherence and phase analysis on smooth surfaces to achieve the same high precision as with PSI but without the fringe-order uncertainty normally associated with narrow-band interferometry.⁵⁻⁸

In practice, combining phase and coherence data for higher precision is quite a tricky procedure and is prone to several sources of uncertainty that can propagate through to a misidentification of fringe order. For example, Harasaki and Wyant have shown that coherence data are highly sensitive to diffraction, leading to localized spikes or wings at the edges of surface features such as steps and lines.⁹ Pfortner and Schwider also note that dispersion in the beam-splitting prism of a Linnik or Michelson interference objective can create linear, field-dependent distortions that lead to obviously incorrect profiles.¹⁰ Thus a fundamental aspect of modern SWLI techniques is correct identification of fringe order by use of the imperfect agreement between phase and coherence information.

2. Frequency-Domain Analysis

The Zygo New View microscope, introduced in 1993, was the first commercial interference microscope to use coherence information to correct automatically for fringe order in phase data. Data processing for this instrument is accomplished by frequency-domain analysis (FDA),^{11,12} a technique that builds on established methods in the analysis of waveguide structures.¹³ Here we begin with a review of the instrument geometry and the FDA technique for surface profiling.

The authors are with the Zygo Corporation, Laurel Brook Road, Middlefield, Connecticut 06455. P. de Groot's e-mail address is peterd@zygo.com.

Received 20 November 2001; revised manuscript received 9 April 2002.

0003-6935/02/224571-08\$15.00/0

© 2002 Optical Society of America

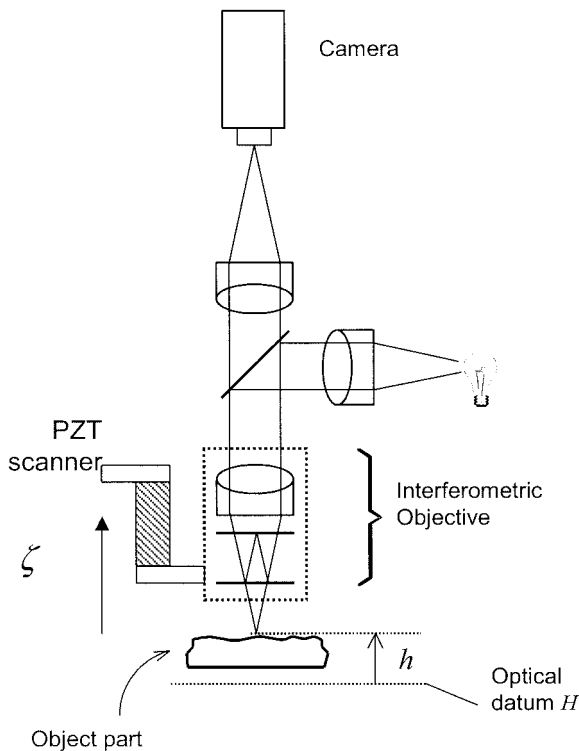


Fig. 1. White-light microscope with a Mirau interference objective for profiling surface heights h with respect to datum plane H by scanning the objective in the ζ direction: PZT, piezoelectric transducer.

Figure 1 is a simplified diagram of a SWLI microscope. The surface has height features $h(x)$ referenced to a fixed optical datum H , where x is an abbreviation for the lateral field position or image pixel number. A computer records intensity data $I(x)$ in successive camera frames during a continuous mechanical scan ζ of the interference objective, often over several tens of micrometers. The $\zeta = 0$ scan position corresponds to zero optical path difference at datum H . To economize on computer memory, we subsample and store for each pixel a 64-frame data trace containing only high-contrast data starting at a scan position $\zeta_{\text{start}}(x)$.¹⁴ In this way we record an array of white-light interference patterns as a function of scan position for multiple image pixels.

One way to model the scan history of the intensity modulation for an individual pixel is to think of it as a collection of single-wavelength fringe patterns superimposed incoherently one upon the other, as shown in Fig. 2. Each fringe pattern has a unique spatial frequency or wave number k , defined here as the rate of change of phase with scan position, e.g., $\sim \pi/2$ rad of phase for the distance scanned between successive camera acquisitions. The peak fringe contrast occurs at a scan position ζ for which the phases of these constituent patterns all agree, corresponding to zero-group-velocity optical path difference. Knowledge of the relative phases of the patterns at any given position in the scan tells us where we are with respect to this zero position.

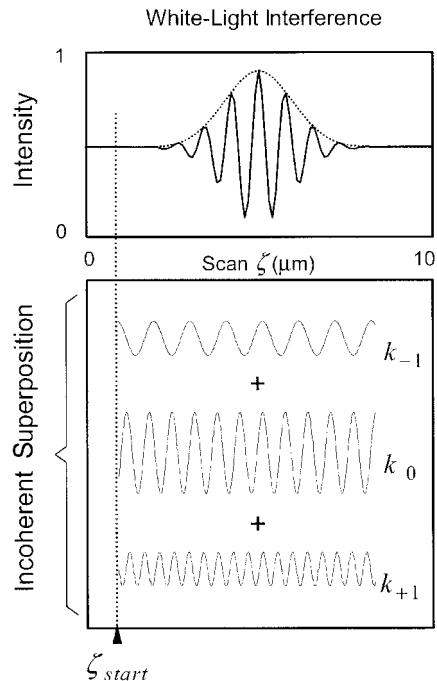


Fig. 2. Conceptual illustration of the mathematical decomposition of a single-pixel white-light interference pattern into multiple-constituent single-wave-number patterns for frequency-domain analysis. Wave number k and corresponding phase ϕ characterize each of the patterns.

It is possible to extract the constituent patterns optically, for example, by means of spectral decomposition with a diffraction grating.¹⁵ However, for full field imaging it is more effective to extract magnitude p and phase ϕ of each constituent pattern mathematically by means of a Fourier transform of the scan history of the white-light interference pattern (see Fig. 3):

$$p(k, x) = |\text{FT}[I(\zeta, x)]|^2, \quad (1)$$

$$\phi''(k, x) = \arg\{\text{FT}[I(\zeta, x)]\}. \quad (2)$$

The double prime for $\phi''(k, x)$ in Eq. (2) means that there is a twofold uncertainty in the fringe order, both from pixel to pixel within the image and overall with respect to datum H . A linear least-squares fit to the phase data weighted by spectral distribution $p(k, x)$ provides for each pixel a slope

$$\sigma(x) \approx d\phi''/dk|_x \quad (3)$$

and an intercept

$$A''(x) \approx \phi''(k = 0, x). \quad (4)$$

Note that intercept $A''(x)$ carries the double prime inherited from the fringe-order uncertainty in the phase data, whereas slope $\sigma(x)$ is free of this uncertainty, provided that neighboring k values in the transform are not too widely separated. Note that to perform this fit we need calculate only a few phase values $\phi''(k, x)$ for each pixel, corresponding to high amplitudes $p(k, x)$, so a limited Fourier transform

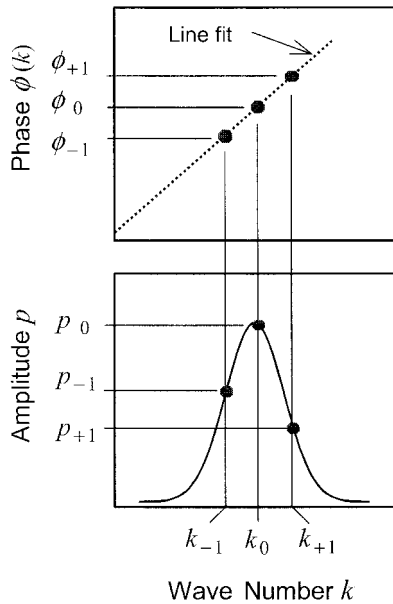


Fig. 3. Results of a Fourier transform of a white-light interference pattern. The phase evolution as a function of wave number is summarized by the linear fit, weighted by amplitudes p .

typically involving only three to seven discrete values of k is sufficient, depending on the source spectral bandwidth, thus economizing on processing time.

Now we turn to the interpretation of the phase data for surface profiling. A general model of a linear phase dependence on wave number k about a nominal value k_0 is

$$\phi(k, x) = k[h(x) - \zeta_{\text{start}}(x)] + (k - k_0)\tau(x) + \gamma(x). \quad (5)$$

Offset $\tau(x)$ accounts for the residual wave-number dependence of the phase when $h(x) = \zeta_{\text{start}}(x)$. This offset will be recognized as linear dispersion, an important but frequently neglected effect in white-light interferometers. Offset $\gamma(x)$ relates to phase bias and phase change on reflection phenomena. Figure 4 is a detailed frequency-domain diagram that incorporates these definitions. Figure 5 shows the corresponding white-light interference pattern that results from the sum over a broad spectral range of individual interference patterns that have a linear phase dependence as in Eq. (5).

There are two ways to extract surface height from linear frequency-domain phase information. A fine-scale calculation of surface-height profile, obtained by direct inversion of Eq. (5) for $k = k_0$, is

$$h(x) = [\theta(x) - \gamma(x)]/k_0, \quad (6)$$

where $\theta(x)$ is the phase profile at k_0 , given by

$$\theta(x) = \theta''(x) - 2\pi M''(x), \quad (7)$$

where

$$\theta''(x) = k_0\zeta_{\text{start}}(x) + k_0\sigma(x) + A''(x) \quad (8)$$

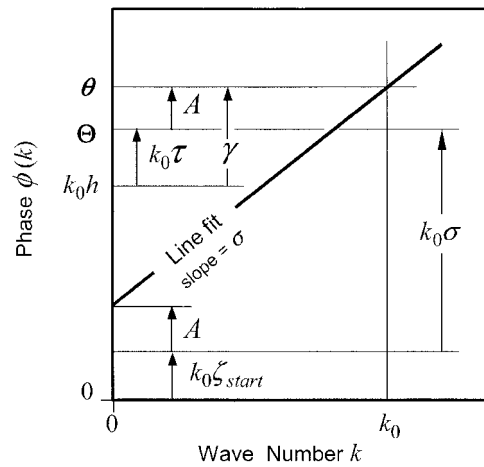


Fig. 4. Frequency-domain portrait of a white-light interference pattern for a single image pixel, showing how coherence profile Θ and phase profile θ relate to surface height h . Note dispersion and phase offsets τ and γ and phase gap A .

and where fringe order $M''(x)$ is initially unknown. In conventional PSI a 2π unwrapping or connect algorithm removes the field or x -dependent portion of $M''(x)$ by comparing height values at neighboring pixels. This is no longer possible when there are steps, high slopes, or significant roughness in the object surface.

This is where the coherence information comes in. Taking the derivative of Eq. (5) and noting that relation (3) holds for slope $\sigma(x)$, we find that

$$h(x) = \Theta(x)/k_0 - \tau(x), \quad (9)$$

where

$$\Theta(x) = k_0\zeta_{\text{start}}(x) + k_0\sigma(x). \quad (10)$$

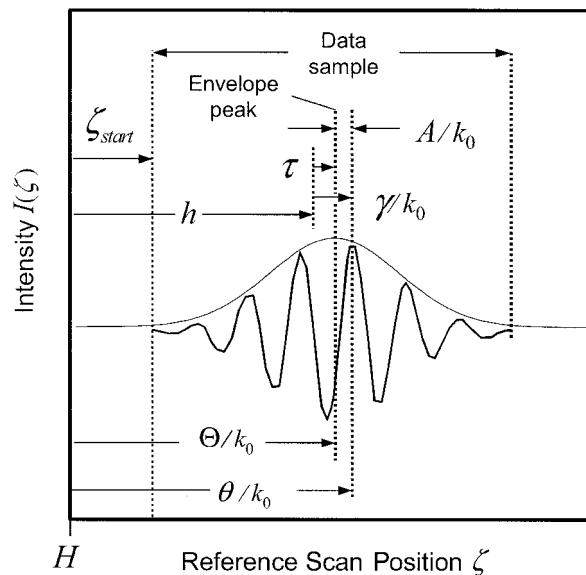


Fig. 5. Intensity-domain portrait of a white-light interference pattern for a single image pixel, showing the meaning of the symbols Θ , θ , h , τ , and γ and of phase gap A to aid in the interpretation of Fig. 4.

This is the coherence profile, in units of phase, and is closely related to the location of the fringe-contrast peak for each image pixel. Unlike the phase itself, coherence profile $\Theta(x)$ is free of fringe order uncertainty $M''(x)$, although it is less precise. The idea therefore is to use coherence to determine the fringe order for each pixel in the phase profile and in this way to achieve high resolution over a large measurement range.

3. Fringe-Order Determination

To find the correct fringe order by using coherence information we analyze the difference between the phase and coherence profiles for the same data acquisition. From Eqs. (8) and (10) we see that this difference is given by the intercept of the linear fit in the frequency domain:

$$A''(x) = \theta''(x) - \Theta(x). \quad (11)$$

We therefore redefine $A''(x)$ as the phase gap, because it quantifies in units of phase the difference between the two ways of profiling the same surface.

Although the experimentally obtained phase gap $A''(x)$ has an uncertain fringe order, we can in principle calculate directly from Eqs. (6), (9), and (11) a theoretical phase gap $A(x)$ free of fringe-order uncertainty, provided that we know the phase and dispersion offsets, $\gamma(x)$ and $\tau(x)$, respectively:

$$A(x) = \gamma(x) - k_0\tau(x). \quad (12)$$

A simple formula for determining fringe order is consequently

$$2\pi M''(x) = A''(x) - A(x). \quad (13)$$

In practice, the exact values of offsets $\gamma(x)$ and $\tau(x)$ are often uncertain, and our *a priori* knowledge of theoretical phase gap $A(x)$ is incomplete. We therefore rely on an empirical technique for estimating or approximating the theoretical phase gap. We call this procedure phase-gap analysis, which has been a significant part of our software development for SWLI over the years since FDA was introduced.

In phase-gap analysis we substitute for $A(x)$ a filtered and connected copy $\alpha'(x)$ of experimental phase gap $A''(x)$. Note the single prime in $\alpha'(x)$, indicating that this procedure removes 2π pixel-to-pixel phase steps but leaves an overall fringe-order uncertainty with respect to H , which we shall set aside for later consideration.

In the simplest approach to approximating the phase gap we calculate a constant average value α'_{avg} over the entire field, using

$$\alpha'_{\text{avg}} = \arctan 2(\bar{C}, \bar{S}), \quad (14)$$

$$S(x) = \sin[A''(x)], \quad (15)$$

$$C(x) = \cos[A''(x)]. \quad (16)$$

The bars over the sine and cosine values in Eq. (14) indicate conventional averaging (sum divided by the number of values) over all valid data points within

the region of interest. Then, from Eq. (13), a fringe-order map $M'(x)$ that is valid to a common fringe order with respect to datum H is

$$M'(x) = \text{Int} \left[\frac{A''(x) - \alpha'(x)}{2\pi} \right], \quad (17)$$

where the Int function returns the nearest integer to its argument. Recalling Eq. (6), we can now write a formula for the surface profile that has the same precision as phase data but without fringe-order uncertainty between pixels:

$$h'(x) = (1/k_0)[\theta''(x) - \gamma(x) - 2\pi M'(x)]. \quad (18)$$

With some differences in notation, Eq. (18) is the original FDA fringe-order algorithm introduced in Refs. 5 and 11.

4. Phase-Gap Analysis

The simple averaging technique of the original FDA algorithm assumes that the theoretical phase gap $A(x)$ is nearly constant over the field of view. However, in practice we have found that there are frequently distortions in the phase gap that are attributable to the x field dependence of phase and dispersion offsets $\gamma(x)$ and $\tau(x)$. Some of the more frequently observed phase gaps are catalogued in Table 1. In these cases the simple averaging technique to approximate $A(x) \approx \alpha'_{\text{avg}}$ is an oversimplification that can lead to misidentification of fringe order.

A more general approach to connecting phase gap $A''(x)$ is to apply one of the many known techniques for adding or subtracting 2π to data in adjacent pixels. This approach preserves the general form of the phase gap, so one can separate the fringe order from imperfections that are traceable to the coherence profile. The connected phase gap is expected to deviate only slightly from the ideal flat surface, and it is therefore feasible and advisable to introduce a significant amount of lateral filtering into this process.

The first level of filtering is on the coherence profile itself. The idea here is that the coherence data, because of diffraction effects, are not capable of accurately profiling sharp edges. Therefore, in Eq. (11) a slightly filtered equivalent $\Theta_{\text{sm}}(x, y)$ replaces $\Theta(x)$, calculated as follows: First locate the edges in the coherence profile, using

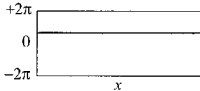
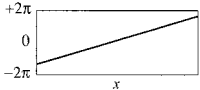
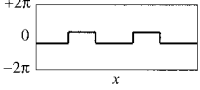
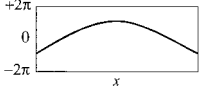
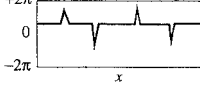
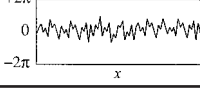
$$\delta\Theta(x, y) = \Theta(x, y) - \text{smooth}[\Theta(x, y)], \quad (19)$$

where smooth is a function that filters data by using, e.g., a single pass of a 3×3 pixel averaging filter or the like. Next, place some limits, e.g., $\pm\pi/2$, on $\delta\Theta(x, y)$ such that we do not overdo the edge smoothing on deep steps. Then

$$\Theta_{\text{sm}}(x, y) = \Theta(x, y) - \delta\Theta(x, y). \quad (20)$$

This algorithm limits smoothing effects to less than one-quarter phase cycle to protect real features in the coherence profile while suppressing diffraction spikes. We then calculate phase gap $A''(x)$, using the smoothed coherence profile in Eq. (11).

Table 1. Possible Appearance and Interpretation of Phase Gap $A''(x)$ after Phase Connection of Pixels

Appearance	Two-Dimensional Profile	Interpretation
Constant over the field of view		This is the ideal case: constant regardless of surface form or features
Overall tip or tilt		Unbalanced wedge dispersion in cube beam splitter (Michelson and Linnik objectives)
Steps that appear to correlate to changes in materials or films		Differences in phase change on reflection between surface regions
Shape that correlates to surface form		Surface-slope-dependent distortions related to optical aberrations
Spikes		Residual effects of diffraction at sharp edges of surface features, e.g., steps
Noise		Surface roughness, optical speckle, or extremely low signal level

The next step is to unwrap or connect phase-gap data $A''(x)$:

$$A'(x) = \text{connect}[A''(x)]. \quad (21)$$

Although any one of several connecting strategies is appropriate, our favored approach sorts the pixels into a queue before the connection, according to the noise level of the surrounding pixels. Sometimes referred to as the quality-guided path technique, this algorithm connects pixels with lowest noise first, then progresses through all the pixels according to increasing noise level.¹⁶ Central to this approach is a merit or confidence function $W(x)$ based on the noise level, ranging from zero for low-quality pixels to $W = 1$ for the ideal case of zero noise. We calculate the confidence function by calculating the mean deviation of nine neighboring pixels from the average value and rescaling to the $W = 0 \dots 1$ range. Pixels that have confidence levels below a threshold W_{\min} are left unconnected, and for these pixels the value of A' is set simply to the average value α'_{avg} and the confidence value is set equal to W_{\min} . Note that for data that have a great deal of noise, for example, data from a rough surface, the algorithm reverts to the simple case of a constant average value α'_{avg} over the entire field, a reasonable default condition.

It is not unusual to have a mixture of noise levels across an object surface that correspond to differences in surface texture, complex surface features, or variable light level. As a consequence, connected phase gap $A'(x)$ may have a large number of unconnected pixels below threshold W_{\min} , resulting in lost data. A postconnect processing step to bring together potentially isolated surface regions that have different noise levels suggests itself, as follows. It is

often the case that the overall shape of the connected phase gap can be approximated by a surface fit. The essential idea therefore is to fit a three-dimensional surface function $\alpha'_{\text{FIT}}(x, y)$ to the connected data. The simplest kind of fit is a plane fit, which can accommodate linear tip and tilt of the coherence profile, which are often traceable to uncompensated dispersion in Michelson objectives. The surface fit makes it possible to recover or fill in for unconnected phase-gap data.

For more-complex shapes and structures in the phase gap beyond tip and tilt, we remark from Table 1 that surface-slope-dependent optical distortions within the instrument often lead to phase-gap characteristics that closely correlate to surface form. Thus an appropriate fitting function for filling unconnected data is

$$\alpha'_{\text{FIT}}(x, y) = c_0 + c_1x + c_2y + c_3\Theta(x, y). \quad (22)$$

We fit this function to the connected phase gap, using a weighted least-squares technique for which the coefficients $c_0 \dots c_3$ are free parameters. The resultant matrix equation is

$$\begin{pmatrix} c_0 \\ c_1 \\ c_2 \\ c_3 \end{pmatrix} = \begin{bmatrix} \langle 1 \rangle & \langle x \rangle & \langle y \rangle & \langle \Theta \rangle \\ \langle x \rangle & \langle x^2 \rangle & \langle xy \rangle & \langle x\Theta \rangle \\ \langle y \rangle & \langle xy \rangle & \langle y^2 \rangle & \langle y\Theta \rangle \\ \langle \Theta \rangle & \langle x\Theta \rangle & \langle y\Theta \rangle & \langle \Theta^2 \rangle \end{bmatrix}^{-1} \begin{pmatrix} \langle A' \rangle \\ \langle xA' \rangle \\ \langle yA' \rangle \\ \langle \Theta A' \rangle \end{pmatrix}, \quad (23)$$

where

$$\langle f \rangle = \sum_{x,y} W(x) f(x). \quad (24)$$

Field-dependent confidence function $W(x)$ in the sum defined by Eq. (24) favors low-noise regions in the fit.

Basis functions for the fit other than $\Theta(x)$ are also worth considering; for example, a simple sphere approximation to the phase gap works well generically for balls and lenses.

As a final step in constructing approximate phase gap $\alpha'(x)$, we balance fit function $\alpha'_{\text{FIT}}(x)$ or blend it with connected phase gap $A'(x)$, using confidence function $W(x)$ as a moderator:

$$\alpha'(x) = \alpha'_{\text{FIT}}(x) + [A'(x) - \alpha'_{\text{FIT}}(x)]W(x)^2. \quad (25)$$

In the high-noise limit $W = W_{\text{min}}$, which usually is encountered on extremely rough surfaces, the phase gap relies heavily on surface-fit value α'_{FIT} . In the low-variance limit the phase gap tends toward the connected value $A'(x)$.

Once we calculate final phase gap $\alpha'(x)$, relative fringe order $M'(x)$ and surface profile $h'(x)$ follow from Eqs. (17) and (18), respectively.

5. Datum-Referenced Profiles

The phase-gap analysis described so far leaves the final profile with an overall phase uncertainty M'_0 with respect to optical datum H :

$$h(x) = h'(x) - \frac{2\pi M'_0}{k_0}, \quad (26)$$

where

$$M'_0 = M(x) - M'(x). \quad (27)$$

If we are interested only in surface form and features, there is no harm in this constant M'_0 and in most cases it may be neglected. This is the most common situation.

There are, however, situations in which knowledge of the overall fringe order is critically important. For these cases we shall need some *a priori* information regarding phase and dispersion offsets $\gamma(x)$ and $\tau(x)$.

The phase and dispersion offsets receive contributions from both the system (subscript sys) and the part itself (subscript part):

$$\gamma(x) = \gamma_{\text{part}}(x) + \gamma_{\text{sys}}(x), \quad (28)$$

$$\tau(x) = \tau_{\text{part}}(x) + \tau_{\text{sys}}(x). \quad (29)$$

Use of a separate procedure involving a known artifact is the best means of determining system contributions $\gamma_{\text{sys}}(x)$ and $\tau_{\text{sys}}(x)$. Part offsets $\gamma_{\text{part}}(x)$ and $\tau_{\text{part}}(x)$, related to the material phase change on reflection and to the rate of change, respectively, are particularly useful for relational measurements between surfaces or surface regions that have dissimilar materials. These values can be calculated directly from knowledge of the optical properties of the surface, for example, the complex index of refraction.

As was noted above, the exact field dependencies of $\gamma(x)$ and $\tau(x)$ are difficult to assess fully, even with some *a priori* information, because of the often unpredictable distortions that are specific to part fea-

tures and slopes. However, for the purpose of determining M'_0 it is in most cases sufficient to know the average values $\bar{\gamma}$ and $\bar{\tau}$. If the distortions in the phase gap are not too severe, we can detect an overall offset M'_0 that is common to all pixels by averaging the approximate phase gap and applying

$$M'_0 = \text{Int} \left[\frac{\bar{\alpha}' - (\bar{\gamma} - k_0 \bar{\tau})}{2\pi} \right]. \quad (30)$$

The final calculation of surface profile with respect to optical datum H with the correct overall fringe order is as in Eq. (26) with Eq. (18).

The most important recent application of datum-referenced profiling is for the measurement of geometric parameters such as thickness and parallelism. A parallel publication describes in detail this unique application of SWLI.¹⁷

6. Examples of Phase-Gap Analysis

As an illustrative example of phase-gap analysis we consider (Fig. 6) the real data sample for a flat surface with a small amount of tilt. Wrapped phase profile $\theta''(x)$ in Fig. 6(a) shows step features of approximately one 2π phase cycle in size. Setting aside for the moment our knowledge of the sample, it cannot be known from wrapped phase profile $\theta''(x)$ alone whether these steps are simply fringe-order errors or actual surface features.

To identify fringe order correctly, we calculate coherence profile $\Theta(x)$ in units of phase at k_0 and then wrapped experimental phase gap $A''(x)$, shown as Figs. 6(b) and 6(c), respectively. Figure 6(d) is the approximate, connected phase gap $\alpha'(x)$ generated with Eq. (25). In this case it has nearly a constant value, indicating that the phase and the coherence data are in good agreement across the field, although there is a small inclination that is perhaps related to a dispersion imbalance in the beam-splitting prism of the Michelson interferometer objective. From the difference of wrapped phase gap $A''(x)$ and its connected copy $\alpha'(x)$ we then calculate, using Eq. (17), Fig. 6(e), which shows the relative fringe order $M'(x)$. Figure 6(f) is the surface height in units of phase at the nominal wave number $k_0 = 2\pi/280$ nm. Thus height $h'(x)$ in Fig. 6 is equal to 280 nm per cycle.

As has been noted, e.g., in Table 1, we often observe phase-gap features that mimic the surface profile to some degree. Such is certainly the case in the example of a sphere in Fig. 7. This is most likely the result of coupling of the surface slope to the off-axis aberrations in the optical system, particularly chromatic aberration, which distorts dispersion offset $\tau(x)$. If it were not for these aberrations, we recall, the phase gap would in the ideal case be perfectly flat, regardless of the actual surface profile. In this case, however, we observe right away in connected phase gap $A''(x)$ a trend in the phase gap that is well approximated by fit $\alpha'_{\text{FIT}}(x)$ of coherence profile $\Theta(x)$, as generated by Eq. (22). Fit $\alpha'_{\text{FIT}}(x)$ fills in the data near the edge of the image that were lost during the

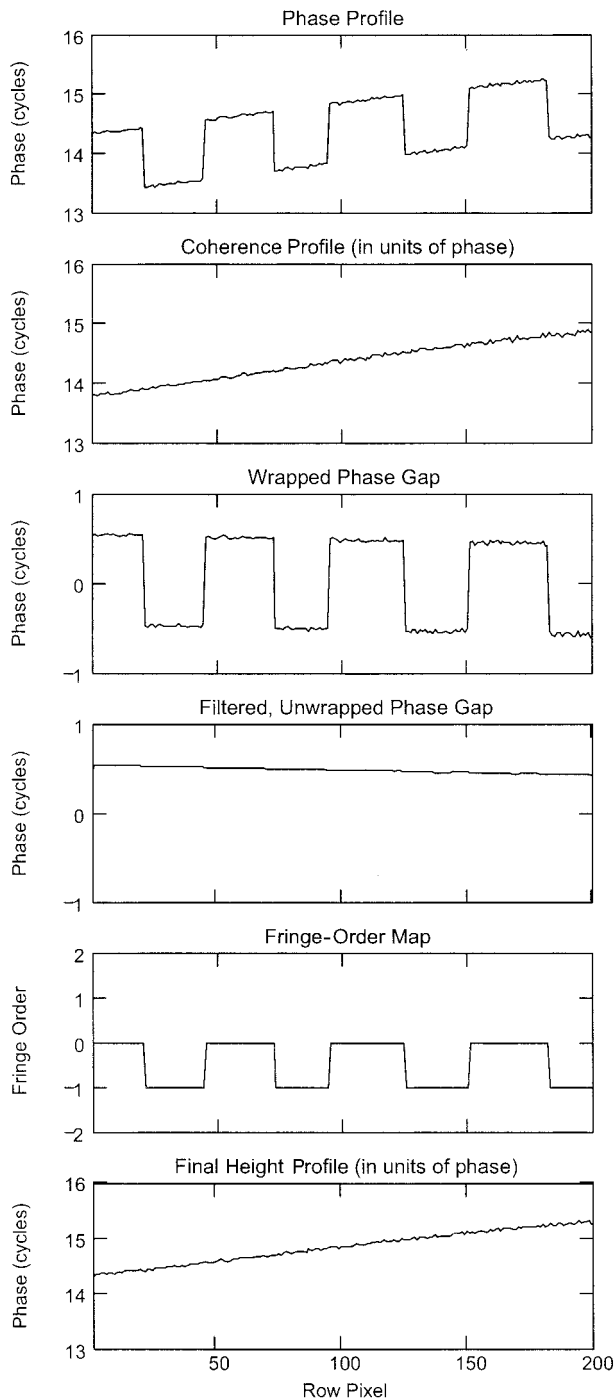


Fig. 6. Example phase-gap analysis of a tilted silicon carbide flat viewed by a SWLI microscope. (a) Wrapped phase profile $\theta''(x)$ and (b) coherence profile $\Theta(x)$ in units of phase at k_0 ; (c) wrapped phase gap $A''(x)$ and (d) filtered, connected phase gap $\alpha'(x)$; (e) fringe-order map $M'(x)$ and (f) final surface height $k_0 h'(x)$, also in units of phase. For the surface height, one phase cycle corresponds to 280 nm.

connect procedure because of noise in the phase gap. The magnitude of the curvature in the final phase gap, $\alpha'(x)$ in Fig. 7, illustrates the importance of a more flexible phase-gap analysis than could be obtained by use of a single average value, which in this

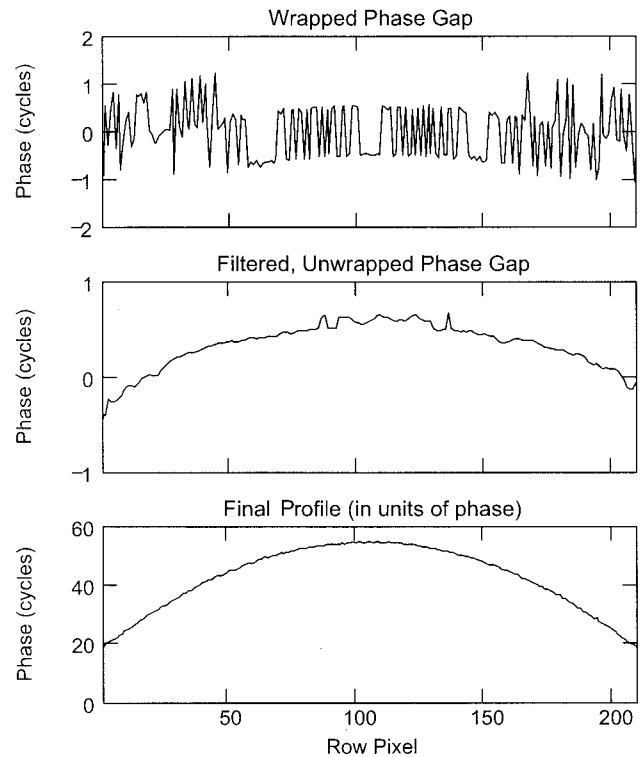


Fig. 7. Example phase-gap analysis of a sphere viewed by a SWLI microscope. After processing, wrapped experimental phase gap $A''(x)$ becomes connected approximate phase gap $\alpha'(x)$ (center). The deviation of $\alpha'(x)$ from perfectly flat is possibly attributable to slope-dependent dispersion $\tau(x)$ in the optical system. The final surface height $k_0 h'(x)$ has units of phase at $k_0 = 2\pi$ cycle/280 nm.

case would have led to errors in fringe-order identification near the edges of the profile.

The example of Fig. 8 in which coherence and phase profiles for a sample with discrete features are compared underscores three points: (1) the significance of diffraction effects in coherence data, (2) the improvement in noise level afforded by high-precision SWLI by use of phase data, and (3) accommodation of thin-film effects. The sample is patterned silicon, and the sharp edges of rectangular features generate spikes that Harasaki and Wyant refer to as "bat wings."⁹ The final profiles generated from phase data do not exhibit these distortions, and the noise level overall is noticeably lower.

7. Discussion

In this paper we have focused on correctly resolving fringe order in high-precision phase data by using frequency-domain analysis; however, the general concept applies to other approaches to generating and combining coherence and phase information. For example, as proposed by Larkin⁶ and by Sandoz *et al.*,⁷ envelope detection techniques can provide coherence profile $\Theta(x)$ while a conventional five- or seven-frame phase-shifting interferometry algorithm centered about the envelope peak provides phase data $\theta''(x)$. Harasaki *et al.* used such an approach, together with an analysis for fringe-order identifica-

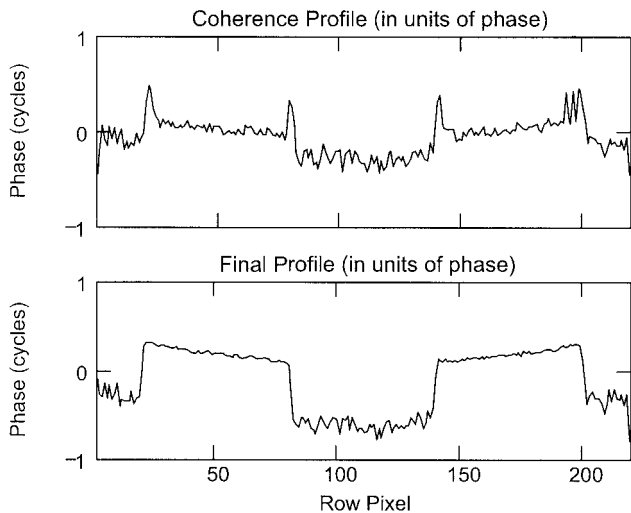


Fig. 8. Comparison of coherence profiling (i.e., fringe localization or envelope peak) with phase profiling by use of coherence only to identify fringe order. The lower, phase-data profile has lower noise and is free of diffraction effects. The sample is patterned silicon.

tion that resembles in some respects our phase-gap connection procedure.¹⁸

Deck and Chakmajian have proposed a variant of the PSI algorithm approach that centers the phase analysis about a common camera frame and represents the mean best focus position for all pixels.¹⁹ This technique exhibits the best performance for shallow surface features because the phase profile relies as closely as possible on interference acquired at a single instant in time, thus greatly reducing sensitivity to vibration, although at the cost of measurement range. Here again, phase-gap analysis is a relevant procedure even though the technique for obtaining the initial phase profile is quite different from that in FDA.

8. Conclusion

Significant differences exist between profiles generated by phase data and by coherence data in scanning white-light interferometry. Resolving these differences is essential when one is using coherence to remove fringe-order uncertainty in phase information. Our approach is to analyze the difference or phase gap between the two techniques, using data filtering, connecting of the phase gap, and surface fitting.²⁰ There are no assumptions of surface continuity, and the algorithm accommodates large step heights or separated surface regions. This technique suppresses potential errors attributable to aberrations, system errors, diffraction effects, and unbalanced dispersion; an additional benefit is its ability to profile with respect to a fixed optical datum H , making it possible to measure relationships between disconnected surfaces.

Although the approach outlined here is sufficient for a large majority of the surface types that we encounter, there is room for improvement in several

special cases, including the handling of thin films and dissimilar materials. The search for such improvement is an active area of continued research in frequency-domain analysis.²¹

References and Notes

1. M. Davidson, K. Kaufman, and I. Mazor, "The coherence probe microscope," *Solid State Technol.* **30**, 57–59 (1987).
2. G. S. Kino and S. S. C. Chim, "Mirau correlation microscope," *Appl. Opt.* **29**, 3775–3783 (1990).
3. T. Dresel, G. Häusler, and H. Venzke, "Three-dimensional sensing of rough surfaces by coherence radar," *Appl. Opt.* **31**, 919–925 (1992).
4. J. C. Wyant, "How to extend interferometry for rough-surface tests," *Laser Focus World* (Sept. 1993), 131–135 (1993).
5. P. de Groot and L. Deck, "Three-dimensional imaging by sub-Nyquist sampling of white-light interferograms," *Opt. Lett.* **18**, 1462–1464 (1993).
6. K. G. Larkin, "Efficient nonlinear algorithm for envelope detection in white-light interferometry," *J. Opt. Soc. Am. A* **4**, 832–843 (1996).
7. P. Sandoz, R. Devillers, and A. Plata, "Unambiguous profilometry by fringe-order identification in white-light phase-shifting interferometry," *J. Mod. Opt.* **44**, 519–534 (1997).
8. P. J. Caber, S. J. Martinek, and R. J. Niemann, "A new interferometric profiler for smooth and rough surfaces," *Laser Dimensional Metrology: Recent Advances for Industrial Application*, M. J. Downs, ed., Proc. SPIE **2088**, 195–203 (1993).
9. A. Harasaki and J. C. Wyant, "Fringe modulation skewing effect in white-light vertical scanning interferometry," *Appl. Opt.* **39**, 2101–2106 (2000).
10. A. Pfortner and J. Schwider, "Dispersion error in white-light Linnik interferometers and its implications for evaluation procedures," *Appl. Opt.* **40**, 6223–6228 (2001).
11. P. de Groot and L. Deck, "Surface profiling by analysis of white-light interferograms in the spatial frequency domain," *J. Mod. Opt.* **42**, 389–401 (1995).
12. P. de Groot, "Method and apparatus for surface topography measurement by spatial-frequency analysis of interferograms," U.S. patent 5,398,113 (14 March 1995).
13. B. L. Danielson and C. Y. Boisrobert, "Absolute optical ranging using low coherence interferometry," *Appl. Opt.* **30**, 2975–2979 (1991).
14. L. Deck, "Method and apparatus for the rapid acquisition of data in coherence scanning interferometry," U.S. patent 5,402,234 (28 March 1995).
15. J. Schwider and L. Zhou, "Dispersive interferometric profilometer," *Opt. Lett.* **19**, 995–997 (1994).
16. D. C. Ghiglia and M. D. Pritt, *Two-Dimensional Phase Unwrapping: Theory, Algorithms and Software* (Wiley, New York, 1998), p. 122.
17. P. de Groot, J. Biegen, J. Clark, X. Colonna de Lega, and D. Grigg, "Optical interferometry for measuring the geometric dimensions of industrial parts," *Appl. Opt.* **41**, 3853–3860 (2002).
18. A. Harasaki, J. Schmit, and J. C. Wyant, "Improved vertical-scanning interferometry," *Appl. Opt.* **13**, 2107–2115 (2000).
19. L. Deck and S. Chakmajian, "Method and apparatus for automatically and simultaneously determining best focus and orientation of objects to be measured by broad-band interferometric means," U.S. patent 5,784,164 (20 March 1997).
20. Improved frequency-domain analysis and phase-gap analysis are the topics of multiple U.S. and foreign patents pending.
21. S.-W. Kim and G.-H. Kim, "Thickness-profile measurement of transparent thin-film layers by white-light scanning interferometry," *Appl. Opt.* **38**, 5968–5973 (1999).